Improving Airborne Lidar Detection of the Subsurface Phytoplankton Layers via a Monte Carlo-Based Correction: A South China Sea Case Study

Mingjia Shangguan, Yirui Guo, Zhongping Lee, *Member, IEEE*, Xiaoquan Song, and Yan He

***Abstract*—Phytoplankton layers are the critical bioenvironmental-coupled dynamic structures in the ocean, playing an essential role in global marine ecosystem functioning and biogeochemical cycles by driving the carbon pump, sustaining energy flow in food webs, and regulating acoustic properties. With its profile detection capability, high vertical resolution, and continuous day-and-night observation, lidar has emerged as an effective tool for detecting phytoplankton layers. However, existing lidar-based inversion algorithms typically rely on specific assumptions and are affected by multiple scattering effects, leading to significant deviations in the inversion results. As an important marginal sea in the western Pacific, the South China Sea, with its unique phytoplankton layer structure, provides valuable insights into regional biophysical coupling mechanisms. In this study, the typical phytoplankton layer in the South China Sea was selected as the research target, and four representative lidar algorithms (i.e., slope method, improved adaptive phytoplankton layer detection method, Klett method, and perturbation method) were systematically analyzed for their effectiveness and applicability in inverting the phytoplankton layer based on a semianalytical Monte Carlo (MC) model. Comparative analysis indicates that the perturbation method is the most effective in extracting key features of the phytoplankton layer, including its depth of maximum and thickness, although significant deviations remain in the thickness inversion. To address this issue, a statistical correction model developed from the semianalytical MC simulation is proposed to amend the perturbation method's results. Airborne lidar experiments were conducted in spring 2024 to demonstrate that the correction model significantly improves the inversion accuracy of phytoplankton layer thickness, with accuracy improvements of 94.8%, 78.9%, 74.6%, and 91.0% at four sampling sites (A_1, A_2, B_1, and B_2) in the South China Sea, respectively. This study provides a novel technology for high-precision lidar inversion of oceanic phytoplankton layers, and is expected to advance research on marine primary productivity and carbon cycling.**

***Index Terms*—Lidar, optical parameter inversion, phytoplankton layer, South China Sea.**

I. Introduction

THE marine ecosystem exhibits significant dynamic complexity [1]. Among its components, phytoplankton—serving as primary producers—play a critical role in marine ecosystems [2], [3]. When phytoplankton aggregate to form thin layers, their photosynthetic activity is substantially enhanced, promoting carbon fixation and oxygen release while influencing the cycling and distribution of nutrients, thereby impacting marine biogeochemical processes [4], [5]. However, the vertical distribution of phytoplankton carries rich environmental information, including temperature [6], salinity [7], and nutrient gradients [8], and also reflects the distribution of water optical parameters [9]. These environmental factors directly affect phytoplankton distribution and growth, making the accurate detection of their vertical distribution essential for unveiling the underlying mechanisms of marine ecological processes [10].

The traditional methods for detecting phytoplankton, such as water sampling and net tows, are labor-intensive and time-consuming and lack sufficient spatial coverage [11]. With the development of remote sensing technology—particularly its advantage in acquiring comprehensive global oceanic information—remote sensing has become an important tool for monitoring marine phytoplankton [12], [13], [14]. Although phytoplankton cells are generally small (typically ranging from less than 1 μm to several hundred micrometers, with most species belonging to the 2–200 μm size range [15], their characteristic pigments (e.g., chlorophyll) exhibit distinct absorption and scattering properties in specific spectral bands, enabling effective detection and monitoring in remote sensing imagery [16]. Passive ocean color remote sensing quantifies surface chlorophyll-*a* concentrations (Chl) by measuring the remote sensing reflectance and applying radiative transfer models and bio-optical inversion algorithms, thereby

Received 16 June 2025; revised 11 October 2025 and 10 November 2025; accepted 29 November 2025. Date of publication 2 December 2025; date of current version 11 December 2025. This work was supported in part by the National Natural Science Foundation of China under Grant 42476184, in part by the National Key Research and Development Program of China under Grant 2022YFB3901704, in part by the Fundamental Research Funds for the Central Universities under Grant 20720200107, and in part by Xiamen Natural Science Foundation General Project under Grant 3502Z202473033. *(Mingjia Shangguan and Yirui Guo contributed equally to this work.)* *(Corresponding authors: Mingjia Shangguan; Xiaoquan Song.)*

Mingjia Shangguan, Yirui Guo, and Zhongping Lee are with the State Key Laboratory of Marine Environmental Science, College of Ocean and Earth Sciences, Xiamen University, Xiamen 361101, China (e-mail: mingjia@xmu.edu.cn).

Xiaoquan Song is with the College of Marine Technology, Faculty of Information Science and Engineering, Ocean University of China, Qingdao 266100, China (e-mail: songxq@ouc.edu.cn).

Yan He is with the Key Laboratory of Space Laser Communication and Detection Technology, Shanghai Institute of Optics and Fine Mechanics, Chinese Academy of Sciences, Shanghai 201800, China.

Digital Object Identifier 10.1109/TGRS.2025.3639387

estimating the biomass distribution of upper water column phytoplankton. The provision of long-term, large-scale observational data has greatly enhanced our understanding of the spatiotemporal distribution of global phytoplankton and their ecological impact on primary production and carbon cycling [17], [18]. However, the passive remote sensing is constrained by illumination conditions, making observations limited under low-light or low-sun-angle environments, and it inherently lacks the capability for vertical profiling measurements [19], [20], [21].

As an active remote sensing technique, lidar is capable of providing continuous, day-and-night vertical distribution information of marine phytoplankton [22], [23], thus serving as an important complement to passive optical remote sensing [24]. In recent years, the application of lidar in detecting phytoplankton layers has garnered extensive attention, with numerous experimental validations conducted on spaceborne, airborne, shipborne, and underwater platforms [25], [26], [27], [28], [29], [30]. However, when detecting phytoplankton layers characterized by stratification, lidar faces an ill-posed inversion problem, requiring the simultaneous retrieval of two unknown parameters: the lidar attenuation coefficient (K_{lidar}) and the backscattering coefficient (β). To address this challenge, various methods have been proposed. Although incorporating additional information, such as Brillouin, Raman, and fluorescence signals, can improve inversion accuracy [29], [31], most lidar systems provide only a single-channel elastic backscatter signal to reduce system complexity, necessitating the use of specific assumptions during the inversion process.

Klett [32] introduces an iterative inversion method that assumes a power-law relationship between K_{lidar} and β to retrieve the K_{lidar} profile. Subsequently, Chen et al. [33] combined the Klett method with the perturbation method—using the former to invert K_{lidar} and the latter for β—demonstrating that the inverted Chl closely matched in situ measurements and revealing the spatiotemporal variability of the phytoplankton layer. Churnside and Marchbanks [34] proposed a perturbation method that simplifies the inversion process by assuming negligible variation of K_{lidar} with depth. While this method achieves less than 10% error in detecting thin phytoplankton layers in oceanic regions with Chl $<$ 1 mg/m^3, it may produce larger errors in nearshore waters with higher Chl. Liu et al. [25] utilized a slope-based approach, extracting the background signal of the lidar return via exponential regression and determining the phytoplankton layer from the signal difference. An airborne experiments in Sanya Bay indicated significant correlations between the inverted phytoplankton layer depth and thickness and the in situ Chl layer parameters.

Despite the satisfactory performance of these algorithms under certain conditions, their overall applicability remains unverified; the validity of the underlying assumptions depends on specific environmental conditions, leading to potential errors that require further correction.

The South China Sea, located in low latitudes with a geographical range from 23°N to the equator and 99°E to 121°E, is the largest marginal sea in the western Pacific. Influenced by the East Asian monsoon and ocean stratification, the surface temperature of the South China Sea exhibits pronounced seasonal variability. In addition to these physical forcings, the widely distributed phytoplankton layers further modulate the thermal structure of the mixed layer through photothermal absorption effects [33], [35], [36]. Numerous studies have shown that subsurface chlorophyll maxima (SCM) are prevalent throughout the South China Sea, with their formation and vertical distribution regulated by multiple physical and biogeochemical factors. Mesoscale eddies influence the vertical structure of the SCM by modulating nutrient transport [37], whereas submesoscale frontal processes control the horizontal redistribution of Chl [38]. Coastal upwelling shoals the SCM and enhances its intensity [39]. In addition, internal waves significantly affect SCM distribution through vertical mixing and nutrient fluxes, particularly in the shallow waters off Taiwan, where internal-wave-induced upwelling transports deep nutrients into the euphotic layer, thereby promoting phytoplankton growth [40]. Therefore, the typical phytoplankton layer distribution in the South China Sea not only provides a robust basis for assessing the applicability of inversion algorithms but also offers critical insights into marine primary production, carbon cycling, and global climate change [33], [41].

Within this background, the study focuses on a typical springtime phytoplankton layer in the South China Sea. Initially, the performance of four representative phytoplankton layer inversion algorithms was systematically evaluated using airborne lidar data. Subsequently, to address the significant discrepancies observed in the results of the best-performing perturbation method, a statistical correction model was developed based on semianalytical Monte Carlo (MC) simulations. Finally, the proposed correction model was validated using airborne lidar experiments and in situ Chl measurements conducted in the South China Sea during spring 2024, demonstrating its effectiveness in enhancing inversion accuracy.

II. Overview of Phytoplankton Layer Inversion Algorithms

The 532-nm Mie scattering lidar equation can be expressed as

$$P(z) = \frac{B \cdot S_r T_a^2 T_t^2 Q(z)}{(n \cdot H + z)^2} \cdot \beta(z) \cdot \exp\left[-2 \int_0^z K_{\text{lidar}}(y) dy\right] \quad (1)$$

where $P(z)$ represents the received signal power, originating from the scattering of the 532-nm laser wavelength at depth z. B is a constant independent of detection depth z, encompassing factors such as laser pulse energy, detector quantum efficiency, and the transmission efficiency of the optical system for both emission and reception. S_r denotes the telescope's receiving area, while T_a and T_t represent the atmospheric and air-sea interface transmittances, respectively. $Q(z)$ is the geometric overlap factor, which equals 1 for airborne oceanic lidar. The refractive index of seawater, n, is taken as 1.33. H denotes the vertical altitude of the lidar system.

Phytoplankton layers in the water column affect both β and K_{lidar}. Therefore, retrieving β or K_{lidar} is commonly used to detect phytoplankton layers [42], [43], [44], and to extract the depth and thickness of the phytoplankton layer.

Section II introduces four representative algorithms for retrieving phytoplankton layer signals.

A. Slope Method

The slope method applies an exponential fit to the range-corrected lidar backscattered signal profile to extract the background signal and compute its difference, thereby identifying phytoplankton layer characteristics [25]. The specific process is as follows.

First, the lidar backscattered signal undergoes depth correction and logarithmic transformation, yielding the range-corrected signal $S(z)$

$$S(z) = \ln\left[P(z)\cdot(n\cdot H+z)^2\right]. \tag{2}$$

Next, to mitigate surface interference and account for the signal-to-noise ratio (SNR), $S(z)$ within the depth range of 2 m to the truncation point is fit using a linear function to obtain the background signal $S_0(z)$. The phytoplankton layer signal $S_L(z)$ is then derived as the difference between $S(z)$ and $S_0(z)$

$$S_L(z) = S(z) - S_0(z). \tag{3}$$

B. Improved Adaptive Phytoplankton Layer Detection Method

This method utilizes curve fitting and robust estimation techniques to extract the phytoplankton layer signal [45]. Initially, the slope method is applied to obtain the $S_L(z)$ signal. However, $S_L(z)$ may still contain noise from sources, such as the seabed, other organic debris, bacteria, and inorganic particles in the water, making it an inadequate representation of the actual underwater phytoplankton layer. Therefore, further noise removal is necessary. A filtering process based on the sample median and absolute deviation is applied to $S_L(z)$ to extract the phytoplankton layer signal.

First, the sample median of $S_L(z)$, denoted as L_E, is determined

$$L_E = \text{median}_{i=1,\ldots,n} S_{L_i}(z). \tag{4}$$

Then, the scale estimate V_E is computed as the product of a correction factor x and the median absolute deviation

$$V_E = x\left(\text{median}_{i=1,\ldots,n}\left|S_{L_i}(z) - L_E\right|\right) \tag{5}$$

where the correction factor x is set to 1.483 to align the estimator with the scale parameter of a Gaussian distribution. The signal $S_L(z)$ is then standardized using L_E and V_E, and the standardized observations $T_i(z)$

$$T_i(z) = \left[S_{L_i}(z) - L_E\right]/V_E. \tag{6}$$

Next, $T_i(z)$ is compared against a cutoff value, with the difference defining the phytoplankton layer detection threshold SUB(z)

$$\text{SUB}(z) = |T_i(z)| - Q_1|T_i(z)| \tag{7}$$

where $Q_1|T_i(z)|$ represents the cutoff value, set as the quartile of the absolute values of the standardized observations $T_i(z)$. A positive SUB(z) is identified as the phytoplankton layer signal $S_L^U(z)$.

C. Klett Method

The Klett method assumes a stable power-law relationship between $\beta(z)$ and $K_{\text{lidar}}(z)$, allowing the lidar equation (1) to be solved and thereby retrieving the $K_{\text{lidar}}(z)$ profile [32]. Specifically, $\beta(z)$ and $K_{\text{lidar}}(z)$ are assumed to satisfy the following relationship:

$$\beta(z) = \text{const}\cdot[K_{\text{lidar}}(z)]^k \tag{8}$$

where const and the exponent k are constants. For elastic lidar, k is set to 1 [46]. Substituting (8) into (1) yields the following expression for $K_{\text{lidar}}(z)$:

$$K_{\text{lidar}}(z) = \frac{\exp\{[S(z) - S(z_d)]/k\}}{[K_{\text{lidar}}(z_d)]^{-1} + \frac{2}{k}\int_z^{z_m}\exp\left[\dfrac{S(y) - S(z_d)}{k}\right]dy} \tag{9}$$

where z_d is the maximum depth after signal truncation, and $K_{\text{lidar}}(z_d)$ is the lidar attenuation coefficient at this depth. Its value is retrieved using the slope method within the interval (z_d − 5 m, z_d) based on the backscattered signal.

D. Perturbation Method

The perturbation method divides the two optical parameters, β and K_{lidar}, into depth-dependent components (perturbation terms, i.e., β', K'_{lidar}) and depth-independent components (non-perturbation terms, i.e., β_0, K^0_{lidar}) [34]. The lidar backscattered signal $S_Z(z)$ after distance correction can be expressed as

$$\begin{aligned} S_Z(z) &= P(z)\cdot(n\cdot H+z)^2 \\ &= C\cdot\left[\beta_0+\beta'(z)\right]\exp\left[-2K^0_{\text{lidar}}z - 2\int_0^z K'_{\text{lidar}}(y)dy\right] \end{aligned} \tag{10}$$

where C represents all constant terms in the lidar equation of (1).

By neglecting the perturbation terms, the background signal $S_Z^0(z)$ is obtained

$$S_Z^0(z) = C\cdot\beta_0\exp\left(-2K^0_{\text{lidar}}z\right). \tag{11}$$

Assuming that $K'_{\text{lidar}}(z)$ can be neglected, the profile of β can be calculated using the following equation:

$$\beta(z) = \frac{S_Z(z)}{S_Z^0(z)}\cdot\beta_0 \tag{12}$$

where β_0 is the nonperturbation term of $\beta(z)$, and is a constant that does not vary with depth. Therefore, its value does not affect the normalized profile shape of $\beta(z)$, allowing for the inversion of the phytoplankton layer information.

The $S_L(z)$, $S_L^U(z)$, $K_{\text{lidar}}(z)$, and $\beta(z)$ obtained using the above methods represent the vertical distribution of the phytoplankton layer. By extracting the peak positions and widths of these profiles, the center depth and thickness of the phytoplankton layer can be retrieved. However, all four inversion algorithms rely on specific assumptions: the slope method and the improved adaptive phytoplankton layer detection method assume vertical homogeneity of the water column, the Klett method assumes a power-law relationship between β and K_{lidar}, and the perturbation method neglects the depth dependence of K_{lidar}.

TABLE I
VERTICAL DISTRIBUTION MODEL OF CHL

Example	Parameter	Value
E_1	f_b	0.01 mg/m^3
	f_p	0.50 mg/m^3
	f_k	0.003 mg/m^4
	z_m	20.00 m
	FWHM	10.00 m
E_2	f_b	0.10 mg/m^3
	f_p	0.70 mg/m^3
	f_k	0.003 mg/m^4
	z_m	40.00 m
	FWHM	20.00 m

On the one hand, due to the complexity of water composition and the high spatiotemporal variability, the applicability of these assumptions is limited. On the other hand, the large amount of multiple scattering that occurs during laser transmission in the water affects both the magnitude and the relationship between β and K_{lidar}. Studies have shown that when the backscattered signal is primarily dominated by single scattering, K_{lidar} approximates the beam attenuation coefficient (c); whereas, when multiple scattering dominates the signal, K_{lidar} approaches the diffuse attenuation coefficient (K_d) [47]. Furthermore, even in a homogeneous water column, K_{lidar} exhibits depth dependence [48], [49]. Therefore, for stratified waters with phytoplankton layer characteristics, all four inversion algorithms introduce errors, leading to a significant reduction in phytoplankton layer inversion accuracy.

III. ASSESSMENT OF FOUR TYPICAL INVERSION ALGORITHMS

To compare and analyze the performance of the four inversion algorithms, particularly their inversion performance in stratified waters with phytoplankton layers, it is first necessary to construct the lidar backscattered signal. The MC method generates many random samples and performs statistical probability analysis, enabling accurate modeling and performance evaluation of complex lidar systems [50], [51], [52], [53], [54]. This method has been experimentally validated and shown to effectively simulate the backscattered signals of ocean lidar systems with significant multiple scattering [55], [56], [57]. Traditional MC simulation methods treat photons as independent particles, simulating their behavior after interacting with the water before reaching the lidar receiver. However, since many photons are required to achieve robust results, the computational demand is extremely high. To improve efficiency, the semianalytical MC method was proposed. Therefore, this study adopts the semianalytical MC simulation method, using the widely applied Petzold scattering phase function. For each scattering event, the expected values are calculated and recorded to obtain the lidar backscattered signal [58], [59], [60]. For details on the simulation method, refer to our group's previous related research [57]. This study focuses on the phytoplankton layer in the South China Sea, using the representative Chl vertical Gaussian distribution model as an example [61]. The standard distribution model is as follows:

$$\text{Chl}(z) = f_p \exp\left[\frac{-(z-z_m)^2}{2\left(\text{FWHM}/2.355\right)^2}\right] + f_k \cdot z + f_b \quad (13)$$

where f_p is the Chl peak value, z_m is the peak position of Chl, f_b represents the Chl baseline value, f_k is the slope of linear variation, and FWHM is the full width at half maximum of the Gaussian model, which corresponds to the thickness of the Chl layer. The specific parameters of the two example models are shown in Table I.

To simplify the modeling, case-1 water type is selected [62]. Based on the Chl vertical Gaussian distribution model, the inherent optical properties (IOPs) of the water are calculated using a bio-optical model, which are then used as input parameters for the MC simulation. The formula is as follows:

$$c(\lambda, \text{Chl}) = a(\lambda, \text{Chl}) + b(\lambda, \text{Chl}) \quad (14)$$

where c, a, and b represent the beam attenuation coefficient, absorption coefficient, and scattering coefficient, respectively, and λ is the emission wavelength, taken as 532 nm. The absorption coefficient a consists of the pure water absorption coefficient a_w, phytoplankton absorption coefficient a_{ph}, and yellow substance absorption coefficient a_y, while the scattering coefficient b includes the pure water scattering coefficient b_w and the particulate scattering coefficient b_p. The empirical models for each optical parameter at 532 nm are shown in Table II [63]

$$a(532, \text{Chl}) = a_w(532) + 0.06A(532) \cdot \text{Chl}^{0.65} + a_y(532, \text{Chl}) \quad (15)$$

$$b(532, \text{Chl}) = b_w(532) + b_p(532, \text{Chl}). \quad (16)$$

In fact, the profile $P(t)$ measured by the ocean lidar is the result of the convolution between the lidar's response function $L(t)$ and the water body response function $W(t)$, and can be expressed as

$$P(t) = L(t) \otimes W(t) \quad (17)$$

where $\otimes$ denotes the convolution operator, and $W(t)$ represents the response of the water body to the laser during its propagation through the water, which can be obtained through MC simulations. $L(t)$ is the lidar's response function, including the effects of pulsewidth, detector response time, and sampling rate of the acquisition card, and can be obtained from the lidar's irradiation on a plane.

An airborne lidar system is employed in this study, with its key parameters listed in Table III. The emitted laser pulse waveform $L(t)$ follows a Gaussian distribution with a width of 8 ns. The system response $W(t)$ is obtained through MC simulations. By combining the simulated $W(t)$ with the known $L(t)$, the lidar profile $P(t)$ is constructed based on (17). During the MC simulation of $W(t)$, to simplify the model and improve computational efficiency, the sea surface is assumed to be calm, and specular reflection from the water surface is neglected.

The measurement dynamic range is limited to 60 dB, meaning signals attenuated to below 10^{-6} are truncated. To

TABLE II
BIO-OPTICAL MODELS OF MC SIMULATION

Parameter	Empirical relationships @532 nm	Reference
a_w	0.045	[64]
a_{ph}	$0.06\times0.453\cdot\text{Chl}^{0.65}$	[65]
a_y	$a_y(440, \text{Chl})\exp[-0.014(532-440)]$	[63]
b_w	2.232×10^{-3}	[66]
b_p	$0.3\cdot\text{Chl}^{0.62}(550/532)$	[67]

TABLE III
KEY PARAMETERS OF LIDAR SYSTEMS

Parameter	Value
Wavelength of laser	532 nm
Photon counts	10^8
Beam spot radius of the emitted laser	25 mm
Laser divergence angle	1 mrad
Aperture of the telescope	200 mm
FOV of the receiver	28 mrad
Tilt angle	15°
Laser pulse width	8 ns
Sample time	1 ns

improve the SNR of the simulated signal, the simulated $W(t)$ is fit using polynomial functions, as shown in Fig. 1 (a-1) and (b-1). Using the fit $W(t), P(t)$ is calculated based on (17). Then, four inversion algorithms are applied to derive $S_L(z), S_L^U(z), K_{\text{lidar}}(z)$, and $\beta(z)$, respectively. To mitigate surface interference, the depth range for linear fitting of the background signal is set from 2 m to the truncation point for the slope method, the improved adaptive phytoplankton layer detection method, and the perturbation method. In the Klett method, the reference depth z_d is set to the truncation point.

Based on the retrieved profiles of $S_L(z), S_L^U(z), K_{\text{lidar}}(z)$, and $\beta(z)$, the peak position (z_m), and FWHM of the scattering layer can be extracted. Taking the β profile as an example, the specific method is illustrated in Fig. 2. Since the Chl profile follows a Gaussian distribution with a baseline and a linear term, as shown in (13), the values of β at the starting and truncation positions are first used for linear fitting, as shown in Fig. 2(a). The linear component is then removed, as shown in Fig. 2(b), followed by baseline subtraction to obtain Fig. 2(c). The resulting data is normalized, and the depth corresponding to the maximum value of the normalized β is identified as z_m, while the width at half maximum corresponds to the FWHM. Using this method, the phytoplankton layer distribution profiles S_P, S_U, S_K, and S_β,derived from $S_L(z), S_L^U(z), K_{\text{lidar}}(z)$, and $\beta(z)$, are compared with the Chl(z) profile, as illustrated in Fig. 1 (a-2) and (b-2).

As shown in Fig. 1 (a-2) and (b-2), when the Chl profile follows a Gaussian distribution, all four inversion algorithms can retrieve the phytoplankton layer information in the water.

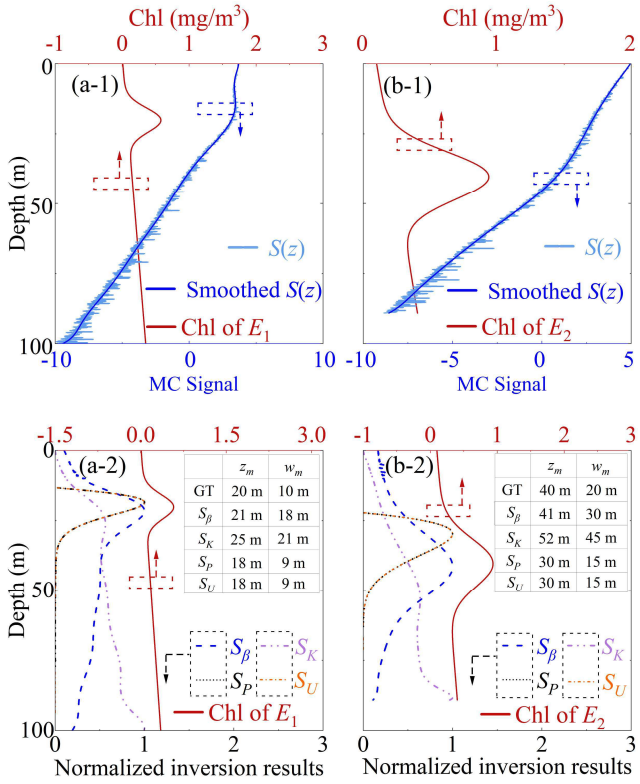

Fig. 1. Vertical Chl distribution profiles and MC-simulated $C(t)$. (a-1) Case with low f_b and shallow z_m. (b-1) Case with high f_b and deep z_m. (a-2) and (b-2) Corresponding phytoplankton layer retrieval results for (a-1) and (b-1), respectively. GT denotes the ground truth, while S_P, S_U, S_K, and S_β represent the normalized results from the slope method, the improved adaptive phytoplankton layer detection method, the Klett method, and the perturbation method, respectively.

However, the retrieved phytoplankton layer center depth (z_m) and thickness both deviate from the true values to varying degrees. Specifically, for water bodies with a low f_p and shallow z_m, as shown in Fig. 1 (a-2), the four inversion algorithms exhibit the following characteristics: the perturbation method achieves the highest accuracy in retrieving z_m, with results closest to the true value. In contrast, the slope method and the improved adaptive phytoplankton layer detection algorithm tend to underestimate z_m, primarily because the background signal $S_0(z)$ inevitably includes part of the actual phytoplankton layer. On the other hand, the perturbation and Klett methods generally overestimate z_m, due to the influence

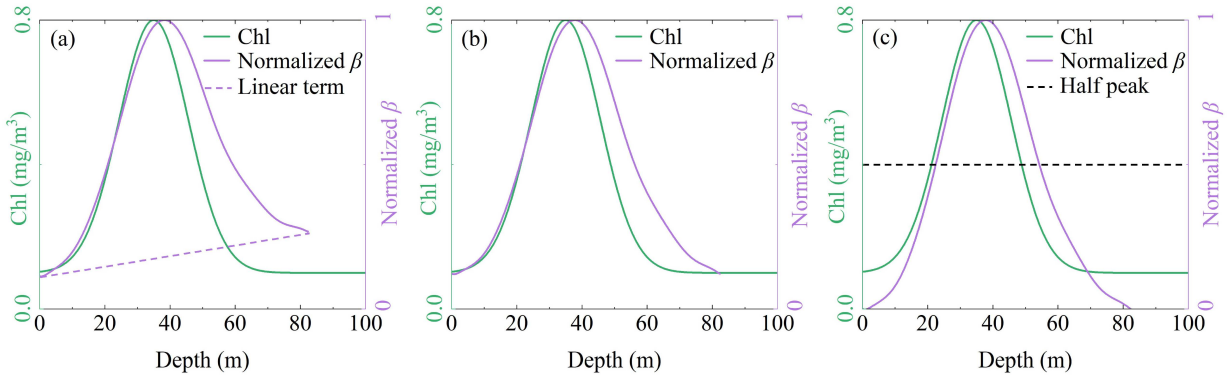

Fig. 2. Schematic of the method for extracting the z_m and FWHM of the phytoplankton layer: (a) original and normalized $\beta(z)$ profiles, (b) $\beta(z)$ profile with the linear term removed, and (c) $\beta(z)$ profile with both the linear term and background value removed. Chl and $\beta(z)$ profiles are shown in green and purple, respectively.

TABLE IV
PARAMETERS FOR MC SIMULATION

Parameter	Value
f_b	0.01 mg/m^3、0.10 mg/m^3
f_p	0.5~10 mg/m^3
f_k	0.003 mg/m^4
z_m	0~60 m
FWHM	1~60 m

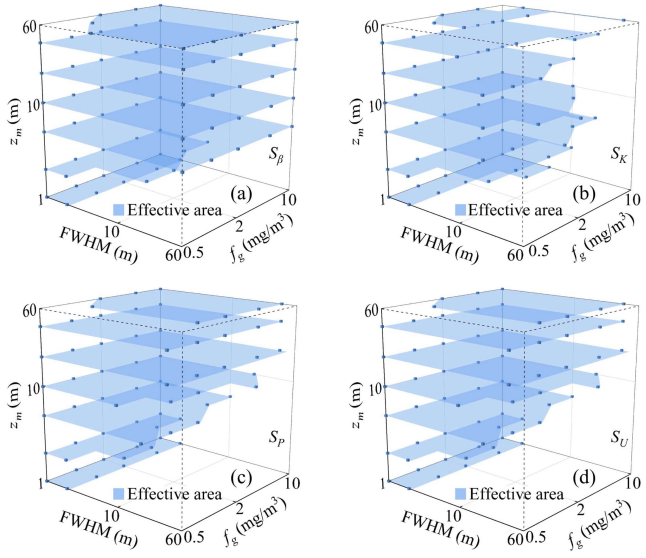

Fig. 3. Effective inversion ranges of four methods for phytoplankton layer detection at f_b = 0.01 mg/m^3: (a) Perturbation method, (b) Klett method, (c) slope method, and (d) improved adaptive phytoplankton layer detection method. Blue dots and shaded areas represent effective inversion regions.

of multiple scattering effects and the limitations of their underlying assumptions.

In terms of FWHM retrieval, the slope method and the improved detection algorithm underestimate the phytoplankton layer thickness, yielding narrower results than the true values, while the perturbation and the Klett methods tend to overestimate the thickness. Similarly, for water bodies with a high f_b and deep z_m, as shown in Fig. 1 (b-2), the four algorithms exhibit the same deviation trends. However, the extent of the deviation increases further due to the enhanced impact of multiple scattering effects.

To further evaluate the performance of the four inversion algorithms, this study uses the Gaussian distribution model described in (13) to construct Chl vertical profiles. By varying the parameters, multiple phytoplankton layer distribution scenarios are simulated, covering depths from shallow (0 m) to deep (60 m), concentrations from low (0.1 mg/m^3) to high (10 mg/m^3), and thickness ranging from 1 to 60 m. The detailed parameter settings are listed in Table IV. Although all four algorithms exhibit certain deviations in their retrieval results, considering that corrections can be applied subsequently, the following statistical analysis focuses primarily on whether the algorithms can successfully extract the phytoplankton layers.

Statistical analysis, as shown in Figs. 3 and 4 reveal the notable differences in the performance boundaries of the four retrieval algorithms. Overall, the perturbation method exhibits the broadest applicability, successfully retrieving phytoplankton layer parameters in 80.82% of the simulated cases, with failure occurring only under extreme conditions where z_m is very shallow (<2 m). In contrast, the Klett method achieves a coverage rate of 57.55%, but performs poorly for phytoplankton layers with large FWHM (>10 m). The slope method and the improved adaptive phytoplankton layer detection method both achieve a coverage rate of 62.45%. Compared to the Klett method, they show improved performance under high-f_p conditions but remain ineffective for thick phytoplankton layers.

As f_b increases, for example, to 0.1 mg/m^3 (see Fig. 4), the effective retrieval region for all algorithms shrinks due to the enhanced impact of multiple scattering, compared to the lower f_b condition of 0.01 mg/m^3. The success rates for the perturbation method, Klett method, slope method,

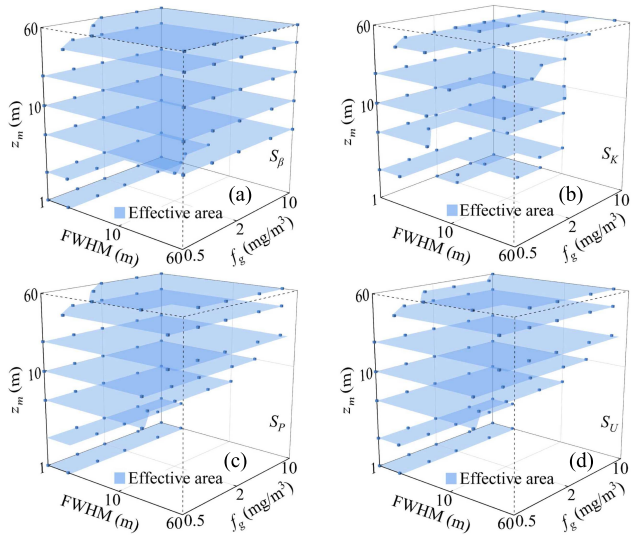

Fig. 4. Effective inversion ranges of four methods for phytoplankton layer detection at f_b = 0.1 mg/m^3: (a) Perturbation method, (b) Klett method, (c) slope method, and (d) improved adaptive phytoplankton layer detection method. Blue dots and shaded areas represent effective inversion regions.

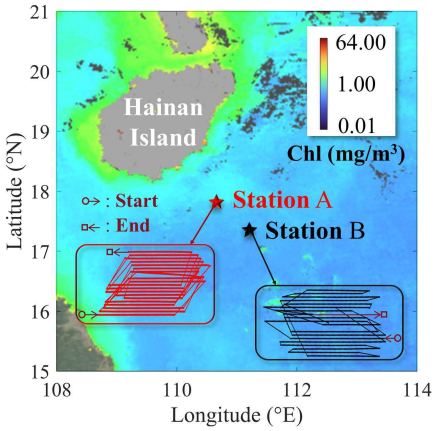

Fig. 5. Distribution of field experiment sites. Pentagrams indicate site locations. Red and black solid lines represent flight trajectories over sites A and B, respectively. Hollow circles and squares denote the start and end points, with arrows indicating flight direction. The background shows the monthly average Chl retrieved from ocean color satellite data.

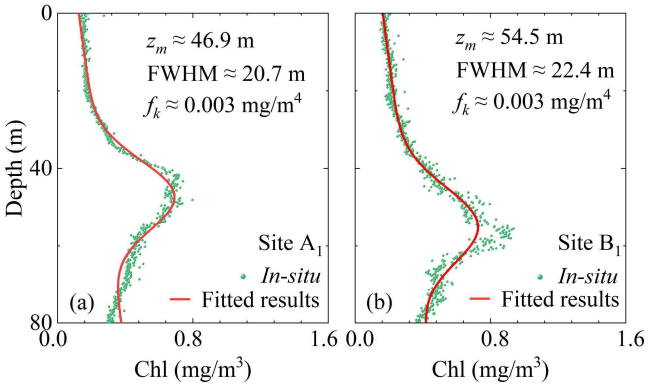

Fig. 6. In situ vertical Chl profiles at stations (a) A_1 and (b) B_1. Dots correspond to the measured data, while the solid lines show the fit profiles based on a Gaussian distribution model.

and improved adaptive method decrease to 79.59%, 46.94%, 62.04%, and 61.22%, respectively. Further analysis indicates that under higher f_b, for deep (z_m > 40 m), low f_p (<1 mg/m^3) layers, peak signals are more likely to be submerged by background noise, reducing the effectiveness of the slope method, the improved adaptive method, and, to a lesser extent, the perturbation method. For the Klett method, accurate retrieval is only achieved in a limited number of cases where the FWHM is small (<10 m) and f_p is high (>1 mg/m^3). Overall, the perturbation method demonstrates the widest applicability and superior performance in retrieving phytoplankton layer characteristics. Accordingly, the perturbation method will be applied to airborne lidar data, and a correction model will be established.

IV. Development of the Correction Model

A. Site Description

In May 2024, an airborne lidar flight experiment was conducted in the adjacent sea area southeast of Hainan Island, along with in situ fluorescence-based measurements of the vertical distribution of Chl. Two observation sites, A and B, were selected for the experiment (indicated by pentagrams in Fig. 5). Site A was observed on May 17, while site B was observed on May 18. The aircraft performed small-scale back-and-forth flights within the areas around sites A and B. The flight trajectories are shown as solid lines in Fig. 5, with arrows indicating the start and end points. The background color in the figure represents the monthly average Chl retrieved from ocean color satellite data for that month, providing a reference for the regional Chl background.

The in situ Chl data reveal that the vertical distribution profiles at fixed observation points A_1 and B_1, located at sites A and B, respectively, exhibit the typical Gaussian-shaped patterns (see Fig. 6), with Chl averaged every 0.1-m interval. At site A_1, the phytoplankton layer exhibited a peak depth (z_m) of approximately 46.9 m with a FWHM of about 20.7 m. In comparison, the phytoplankton layer at site B_1 is deeper ($z_m \approx$ 54.5 m) and slightly thicker (FWHM ≈ 22.4 m). It should be noted that, according to previous studies, the slope for the linear term was generally found to be below zero [68]. However, in our case, the vertical Chl profiles exhibited positive slopes, with f_k of both sites approximately 0.003 mg/m^{-4}. On the one hand, upwelling currents near the northern coast of the South China Sea promote nutrient uplift [69]; on the other hand, as shown in Fig. 6, the limitation of sampling depth (0–80 m) may result in incomplete capture of the deep chlorophyll maximum feature. Similar effects of limited sampling depth have also been reported in previous studies [70]. Based on these in situ Chl measurements, a phytoplankton layer correction model for the South China Sea is subsequently developed using MC simulation.

B. Phytoplankton Layer Correction Model for the South China Sea

Although the perturbation method offers the broadest applicability for extracting the phytoplankton layer, its inversion

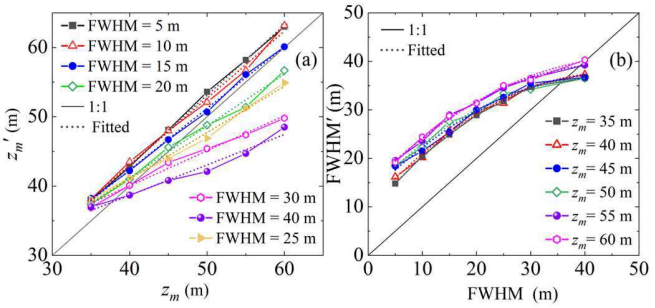

Fig. 7. (a) Relationship between the retrieved phytoplankton layer peak position z_m' and the true peak position z_m under different FWHM conditions. (b) Relationship between the retrieved phytoplankton layer thickness FWHM′ and the true thickness FWHM under different z_m conditions. Dots represent MC simulation results, and dashed lines indicate fit curves.

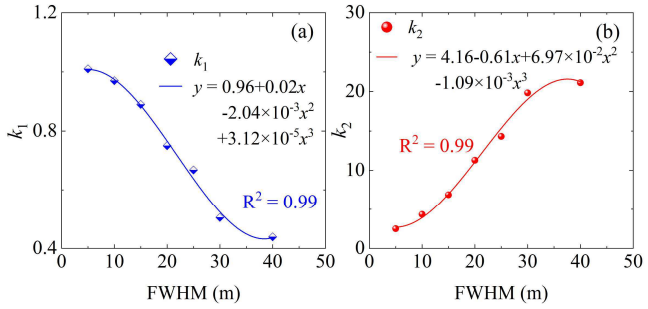

Fig. 8. Polynomial fitting relationships between parameter (a) k_1, (b) k_2, and the FWHM.

results still exhibit deviations, necessitating the development of a corresponding correction model. To this end, based on the vertical Chl distribution characteristics measured in situ at the South China Sea station, a Gaussian Chl profile as defined in (13) is adopted. The background Chl f_b is uniformly set to 0.1 mg/m^3, and the surface Chl f_p is set to 0.7 mg/m^3. The peak depth z_m varies between 35 and 60 m, and FWHM ranges from 5 to 40 m. MC simulations are conducted to analyze the distribution pattern of deviations between the perturbation method inversion results and the true values.

In the simulation, the MC-derived signal $W(t)$ and the known $L(t)$ are first used in (17) to obtain the lidar profile $P(t)$. After correcting for the lidar tilt angle, the perturbation method described in (10)–(12) is applied to retrieve the vertical scattering coefficient profile $\beta(z)$. Then the phytoplankton layer profile S_β is obtained through the processing, as shown in Fig. 2. The depth corresponding to the maximum of S_β is defined as the retrieved phytoplankton layer peak position z_m', and its thickness is taken as the retrieved FWHM (FWHM′). The relationships between z_m' and z_m, as well as FWHM′ and FWHM, are then analyzed. The results are shown in Fig. 7.

From Fig. 7(a), under different FWHM conditions, z_m' and z_m exhibit a consistent monotonic increasing trend. When FWHM is small, the relationship between z_m' and z_m is closer to the 1:1 line; as the FWHM increases, the response of z_m' to z_m becomes more gradual, and the fit curve gradually deviates from the 1:1 line, indicating that the inversion error increases with z_m and becomes more pronounced under larger FWHM

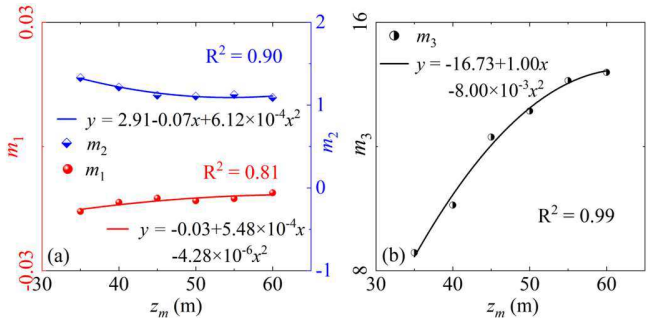

Fig. 9. Polynomial fitting relationships between the coefficients of the quadratic fit of FWHM and FWHM′ (a) m_1 and m_2 and (b) m_3 and z_m.

conditions. To address this, linear fitting is first performed between z_m' and z_m, followed by analyzing the relationship between the fitting parameters and FWHM:

$$z_m = \left(z_m' - k_2\right)/k_1 \tag{18}$$

where k_1 and k_2 represent the slope and intercept of the fit linear function, respectively, and both exhibit a coefficient of determination (R^2) of 0.99. Further analysis reveals a relationship between k_1 and k_2, and the thickness (FWHM), as shown in Fig. 8. The fit relationships are as follows:

$$\begin{cases} k_1 = 0.96 + 0.02 \cdot \mathrm{FWHM} - 2.04 \times 10^{-3} \cdot \mathrm{FWHM}^2 \\ \qquad + 3.12 \times 10^{-5} \cdot \mathrm{FWHM}^3 \\ k_2 = 4.16 - 0.61 \cdot \mathrm{FWHM} + 6.97 \times 10^{-2} \cdot \mathrm{FWHM}^2 \\ \qquad - 1.09 \times 10^{-3} \cdot \mathrm{FWHM}^3. \end{cases} \tag{19}$$

As shown in Fig. 7(b), FWHM′ increases with FWHM, exhibiting consistent trends across different z_m values (35–60 m) with only minor variations. The relationship between FWHM′ and FWHM under each z_m condition is fit using a second-order polynomial. The fit expressions are as follows:

$$\mathrm{FWHM} = \frac{-m_2 + \sqrt{m_2^2 - 4m_1\left(m_3 - \mathrm{FWHM}'\right)}}{2m_1} \tag{20}$$

where m_1, m_2, and m_3 are fitting coefficients, with R^2 values of 0.81, 0.90, and 0.99, respectively. Further analysis reveals relationships between these coefficients and z_m, as shown in Fig. 9. The fit relationships are as follows:

$$\begin{cases} m_1 = -0.03 + 5.48 \times 10^{-4} \cdot z_m - 4.28 \times 10^{-6} \cdot z_m^2 \\ m_2 = 2.91 - 0.07 \cdot z_m + 6.12 \times 10^{-4} \cdot z_m^2 \\ m_3 = -16.73 + 1.00 \cdot z_m - 8.00 \times 10^{-3} \cdot z_m^2. \end{cases} \tag{21}$$

Using (18)–(21), the inverted z_m' and FWHM′ can be obtained as 3-D fit surfaces corresponding to z_m and FWHM, respectively, as shown in Fig. 10. As illustrated in Fig. 10(a), when the phytoplankton layer is thin, z_m' and z_m approximately follow a 1:1 relationship, indicating that the perturbation method can accurately predict the phytoplankton layer depth under thin layer conditions. As FWHM increases, z_m' gradually becomes smaller than z_m, suggesting that the error caused by the simplified assumptions in the perturbation method

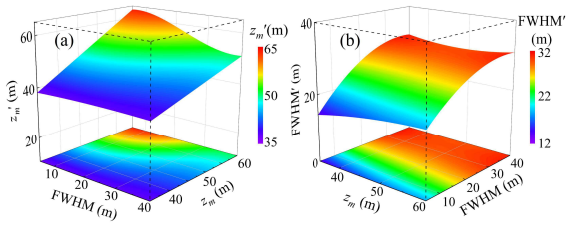

Fig. 10. (a) Relationship of z_m' with z_m and FWHM calculated using (18) and (19). (b) Relationship of FWHM′ with z_m and FWHM calculated using (20) and (21).

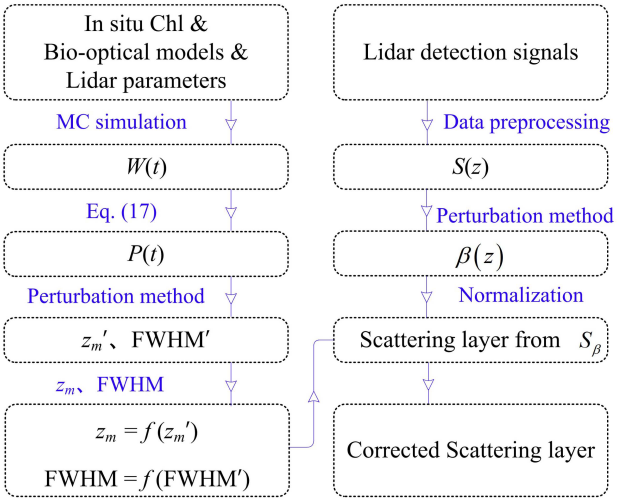

Fig. 11. Flowchart of the correction process.

increases with increasing phytoplankton layer thickness. Furthermore, Fig. 10(b) shows that when the phytoplankton layer thickness is fixed, z_m has a minor effect on FWHM′, indicating that FWHM′ is mainly influenced by FWHM rather than z_m.

To validate the accuracy of the phytoplankton layer correction model, the airborne lidar measured data will be inverted using the perturbation method, followed by correction with (18)–(21) to obtain the corrected parameters (FWHM^C and z_m^C). The correction results are then validated by comparison with in situ Chl data. The detailed process is shown in Fig. 11.

V. Field Measurements

The raw signals measured by the airborne lidar at sites A and B are shown in Figs. 12(a) and 13(a), respectively. The β profiles inverted using the perturbation method are presented in Figs. 12(b) and 13(b). The phytoplankton layers extracted from the β profiles, along with the corrected phytoplankton layers obtained through (18)–(21), are shown in Figs. 12(c) and 13(c). The red line segments indicate the in situ measurements at fixed sites A_1, A_2, B_1, and B_2.

From Figs. 12(c) and 13(c), after correction using the statistical model, the inverted phytoplankton layer center position (z_m^C) and thickness (FWHM^C) are more consistent with the in situ observations. Specifically, the correction based on the inversion results indicates that both z_m and FWHM of the scattering layer have decreased. After correction, the upper boundary of the layer structure remains stable, while the lower

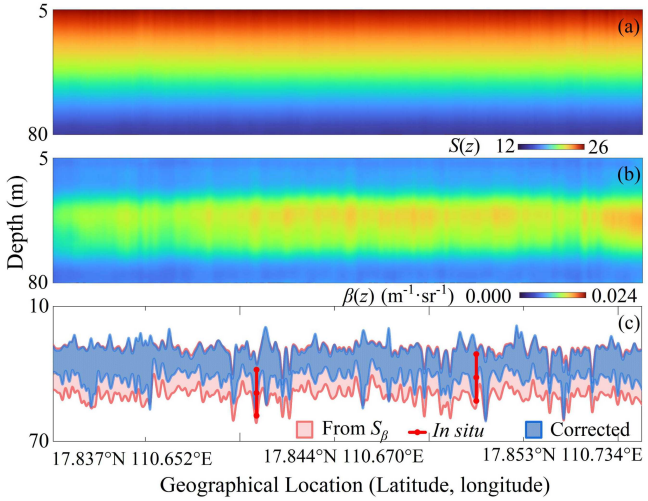

Fig. 12. Field experiment results from airborne lidar at site A. (a) Raw lidar signal $S(z)$. (b) β profile retrieved using the perturbation method. (c) Phytoplankton layer before and after correction. The red shaded area represents the phytoplankton layer derived from the β profile; the blue shaded area shows the corrected phytoplankton layer based on (18)–(21), and the red lines indicate in situ measurements at stations A_1 and A_2.

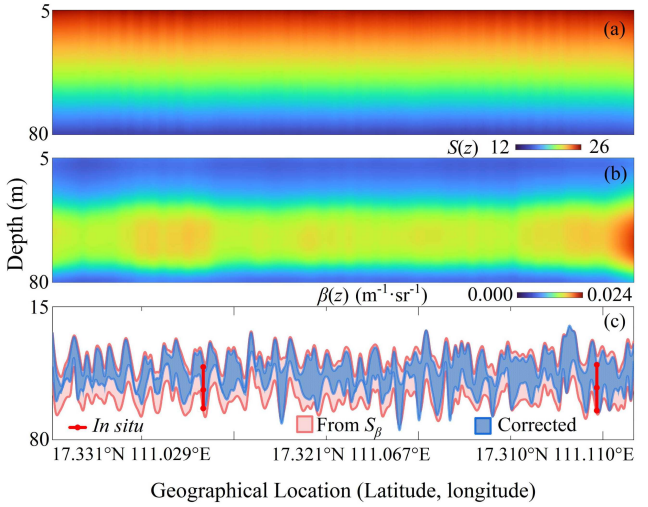

Fig. 13. Field experiment results from airborne lidar at site B. (a) Raw lidar signal $S(z)$. (b) β profile retrieved using the perturbation method. (c) Phytoplankton layer before and after correction. The red shaded area represents the phytoplankton layer derived from the β profile; the blue shaded area shows the corrected phytoplankton layer based on (18)–(21), and the red lines indicate in situ measurements at stations B_1 and B_2.

boundary has risen significantly. As shown in Fig. 12(c), the in situ FWHM values at sites A_1 and A_2 are 20.7 and 20.4 m, respectively. After correction, the estimated thicknesses are substantially reduced from 26.5 and 25.6 m to 20.4 and 19.3 m, with inversion accuracies improved to 94.8% and 78.9%. Similarly, Fig. 13(c) shows that the in situ FWHM values at sites B_1 and B_2 are 22.4 and 20.2 m, and the corrected thicknesses decrease markedly from 27.9 to 26.9 m to 21.0 and 19.6 m, achieving inversion accuracies of 74.6% and 91.0%, respectively. The corrected layer thicknesses closely match the in situ observations, validating the reliability and accuracy of the correction model. Overall, the proposed model

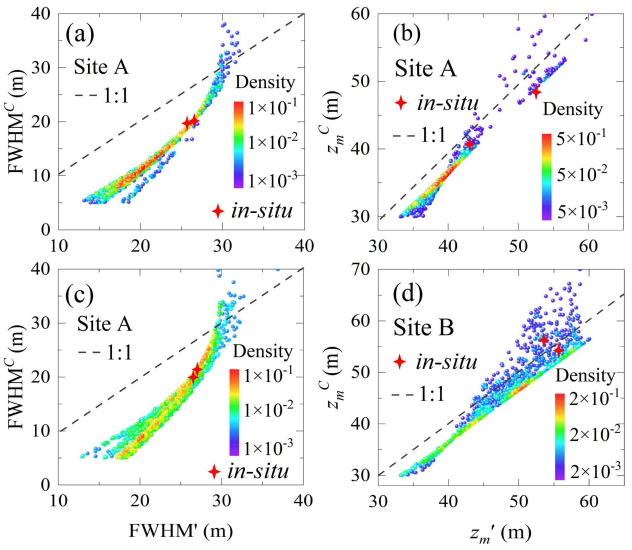

Fig. 14. Density distribution of the relationship between phytoplankton layer results before and after correction at sites A and B. (a) Comparison of FWHM^C and FWHM′ at site A. (b) Comparison of z_m^C and z_m' at site A. (c) Comparison of FWHM^C and FWHM′ at site B. (d) Comparison of z_m^C and z_m' at site B.

significantly improves the estimation accuracy of phytoplankton layer parameters and shows strong potential for application in oceanic phytoplankton layer detection. It is worth noting that the corrected SCM layers in Figs. 12 and 13 both exhibit wave-like oscillations, with the amplitude in Fig. 13 being notably larger than in Fig. 12. Such wave-like variations may be caused by the following factors. On the one hand, internal waves (particularly nonlinear internal waves) are a known physical mechanism that can lead to wavy structures in scattering layers [71]. On the other hand, wind-induced sea surface undulations or sea level anomaly (SLA) variability may also contribute to these oscillations. When the laser beam is incident on a sloped sea surface formed by wind or local SLA variations, the scattering path is deflected, resulting in the observed wave-like height variations of the detected scattering layer [72]. The exact causes of these variations will be further investigated in future experiments.

To better illustrate the correction results, Fig. 14 presents the density distributions of the corrected z_m^C and FWHM^C against the uncorrected z_m' and FWHM. As shown in Fig. 14(a) and (c), the relationship between FWHM^C and FWHM′ is significantly below the 1:1 line under low z_m' conditions, and FWHM^C aligns well with the in situ measurements, indicating that the correction of phytoplankton layer thickness using (20) and (21) is effective. Before correction, the phytoplankton layer thickness ranged between 13 and 35 m; after correction, it narrowed to 5–40 m. In addition, at sites A and B, the phytoplankton layer thickness before correction is mainly concentrated between 20 and 25 m, while after correction it is mostly within 5–15 m. As shown in Fig. 14(b) and (d), the relationship between z_m^C and z_m' generally falls slightly below the 1:1 line, with the phytoplankton layer depth distribution consistent before and after correction, ranging from 35 to 60 m. Specifically, the phytoplankton layer center at site A is concentrated between 35 and 45 m, whereas at site B it is relatively deeper, mostly between 40 and 50 m. This trend agrees well with the in situ measurement results.

VI. Conclusion

This work compares four typical algorithms for extracting ocean phytoplankton layers, including the slope method, an improved adaptive phytoplankton layer detection method, the Klett method, and the perturbation method. Their applicability to typical scattering-layer water bodies in the South China Sea was evaluated. The results show that all four algorithms exhibit retrieval biases, among which the perturbation method demonstrates the broadest applicability for retrieving the depth and thickness of Gaussian-distributed phytoplankton layers. To correct the retrieval biases of the perturbation method, a phytoplankton layer correction model specific to the South China Sea was developed based on a semianalytical MC approach. The effectiveness of this model was validated using airborne lidar measurement data. Although the present study does not encompass all possible types of chlorophyll stratification, the proposed technical framework remains applicable for correcting the chlorophyll layer information retrieved by lidar.

This work provides a new technical pathway for detecting phytoplankton layers in water bodies, though some limitations remain. For example, in highly turbid waters, the influence of multiple scattering effects on retrieval accuracy is not yet fully understood, which restricts the model's applicability in complex environments. However, the proposed correction model is primarily based on data from the South China Sea, and its generalizability to other regions needs further validation. Future work may integrate multispectral lidar and ocean color remote sensing data to further optimize the correction model, improve retrieval accuracy, and expand its scope of application. Overall, this study offers important theoretical and methodological support for the application of lidar technology in marine ecological monitoring and holds significant theoretical significance and application potential.

References

[1] M. J. Fogarty, R. Gamble, and C. T. Perretti, "Dynamic complexity in exploited marine ecosystems," *Frontiers Ecol. Evol.*, vol. 4, p. 68, Jun. 2016.

[2] J. E. Cloern and A. D. Jassby, "Complex seasonal patterns of primary producers at the land–sea interface," *Ecol. Lett.*, vol. 11, no. 12, pp. 1294–1303, Dec. 2008.

[3] L. Guidi et al., "Effects of phytoplankton community on production, size, and export of large aggregates: A world-ocean analysis," *Limnology Oceanogr.*, vol. 54, no. 6, pp. 1951–1963, Nov. 2009.

[4] W. M. Durham and R. Stocker, "Thin phytoplankton layers: Characteristics, mechanisms, and consequences," *Annu. Rev. Mar. Sci.*, vol. 4, no. 1, pp. 177–207, Jan. 2012.

[5] A. H. Taylor, A. J. Watson, M. Ainsworth, J. E. Robertson, and D. R. Turner, "A modelling investigation of the role of phytoplankton in the balance of carbon at the surface of the North Atlantic," *Global Biogeochemical Cycles*, vol. 5, no. 2, pp. 151–171, Jun. 1991.

[6] F. Gessner, "The vertical distribution of phytoplankton and the thermocline," *Ecology*, vol. 29, no. 3, pp. 386–389, Jul. 1948.

[7] M. Ahel, R. Barlow, and R. Mantoura, "Effect of salinity gradients on the distribution of phytoplankton pigments in a stratified estuary," *Mar. Ecol. Prog. Ser.*, vol. 143, pp. 289–295, Nov. 1996.

[8] K. Richardson and J. Bendtsen, "Vertical distribution of phytoplankton and primary production in relation to nutricline depth in the open ocean," *Mar. Ecol. Prog. Ser.*, vol. 620, pp. 33–46, Jun. 2019.

[9] M. J. Behrenfeld and E. Boss, "Beam attenuation and chlorophyll concentration as alternative optical indices of phytoplankton biomass," *J. Mar. Res.*, vol. 64, no. 3, pp. 431–4512006.

[10] J. E. O'Reilly et al., "Ocean color chlorophyll algorithms for SeaWiFS," *J. Geophys. Research: Oceans*, vol. 103, no. C11, pp. 24937–24953, Oct. 1998.

[11] P. Donaghay, H. Rines, and J. M. Sieburth, "Simultaneous sampling of fine scale biological, chemical, and physical structure in stratified waters," *Ergebnisse Der Limnologie*, vol. 36, pp. 97–108, 1992.

[12] I. M. Belkin, "Remote sensing of ocean fronts in marine ecology and Fisheries," *Remote Sens.*, vol. 13, no. 5, p. 883, Feb. 2021.

[13] D. Blondeau-Patissier, J. F. R. Gower, A. G. Dekker, S. R. Phinn, and V. E. Brando, "A review of ocean color remote sensing methods and statistical techniques for the detection, mapping and analysis of phytoplankton Blooms in coastal and open oceans," *Prog. Oceanogr.*, vol. 123, pp. 123–144, Apr. 2014.

[14] V. Klemas and X.-H. Yan, "Subsurface and deeper ocean remote sensing from satellites: An overview and new results," *Prog. Oceanogr.*, vol. 122, pp. 1–9, Mar. 2014.

[15] V. Montecino and D. Quiroz, "Specific primary production and phytoplankton cell size structure in an upwelling area off the coast of Chile (30° S)," *Aquatic Sci.*, vol. 62, no. 4, pp. 364–380, Dec. 2000.

[16] I. Joint and S. B. Groom, "Estimation of phytoplankton production from space: Current status and future potential of satellite remote sensing," *J. Experim. Mar. Biol. Ecol.*, vol. 250, nos. 1–2, pp. 233–255, Jul. 2000.

[17] S. Alvain, C. Moulin, Y. Dandonneau, and H. Loisel, "Seasonal distribution and succession of dominant phytoplankton groups in the global ocean: A satellite view," *Global Biogeochemical Cycles*, vol. 22, no. 3, Sep. 2008, Art. no. GB3001.

[18] A. Bracher et al., "Obtaining phytoplankton diversity from ocean color: A scientific roadmap for future development," *Frontiers Mar. Sci.*, vol. 4, p. 55, Mar. 2017.

[19] B. Collister et al., "Assessing the utility of high spectral resolution LiDAR for measuring particulate backscatter in the ocean and evaluating satellite ocean color retrievals," *Remote Sens. Environ.*, vol. 300, Jan. 2024, Art. no. 113898.

[20] Z. Zhang et al., "Consistency analysis of water diffuse attenuation between ICESat-2 and MODIS in marginal sea: A case study in China sea," *Remote Sens. Environ.*, vol. 318, Mar. 2025, Art. no. 114602.

[21] X. Li, P. Chen, Z. Zhang, Y. Li, and D. Pan, "Vertical structure observation from spaceborne LiDAR ICESat-2 in East China Sea," *Opt. Exp.*, vol. 33, no. 2, pp. 2847–2865, 2025.

[22] J. A. Schulien et al., "Vertically-resolved phytoplankton carbon and net primary production from a high spectral resolution LiDAR," *Opt. Exp.*, vol. 25, no. 12, pp. 13577–13587, 2017.

[23] J. H. Churnside, R. D. Marchbanks, and N. Marshall, "Airborne LiDAR observations of a spring phytoplankton Bloom in the western Arctic ocean," *Remote Sens.*, vol. 13, no. 13, p. 2512, Jun. 2021.

[24] A. Willitsford and C. R. Philbrick, "LiDAR description of the evaporative duct in ocean environments," *Proc. SPIE*, vol. 5885, pp. 140–147, Aug. 2005.

[25] H. Liu, P. Chen, Z. Mao, D. Pan, and Y. He, "Subsurface plankton layers observed from airborne LiDAR in Sanya bay, South China Sea," *Opt. Exp.*, vol. 26, no. 22, pp. 29134–29147, 2018.

[26] P. Chen, Z. Mao, Z. Zhang, H. Liu, and D. Pan, "Detecting subsurface phytoplankton layer in Qiandao lake using shipborne LiDAR," *Opt. Exp.*, vol. 28, no. 1, pp. 558–569, 2020.

[27] H. Zheng et al., "Deriving vertical profiles of chlorophyll—A concentration in the upper layer of seawaters using ICESat-2 photon-counting LiDAR," *Opt. Exp.*, vol. 30, no. 18, pp. 33320–33336, 2022.

[28] M. Shangguan, Y. Guo, and Z. Liao, "Shipborne single-photon fluorescence oceanic LiDAR: Instrumentation and inversion," *Opt. Exp.*, vol. 32, no. 6, pp. 10204–10218, 2024.

[29] M. Shangguan, Z. Liao, and Y. Guo, "Simultaneous sensing profiles of beam attenuation coefficient and, volume scattering function at 180° using a single-photon underwater elastic-Raman LiDAR," *Opt. Exp.*, vol. 32, no. 5, pp. 8189–8204, 2024.

[30] J. Churnside, B. McCarty, and X. Lu, "Subsurface ocean signals from an orbiting polarization LiDAR," *Remote Sens.*, vol. 5, no. 7, pp. 3457–3475, Jul. 2013.

[31] M. Shangguan et al., "Sensing profiles of the, volume scattering function at 180° using a single-photon oceanic fluorescence LiDAR," *Opt. Exp.*, vol. 31, no. 24, pp. 40393–40410, 2023.

[32] J. D. Klett, "Stable analytical inversion solution for processing LiDAR returns," *Appl. Opt.*, vol. 20, no. 2, pp. 211–220, 1981.

[33] P. Chen et al., "Vertical distribution of subsurface phytoplankton layer in South China Sea using airborne LiDAR," *Remote Sens. Environ.*, vol. 263, Sep. 2021, Art. no. 112567.

[34] J. H. Churnside and R. D. Marchbanks, "Inversion of oceanographic profiling LiDARs by a perturbation to a linear regression," *Appl. Opt.*, vol. 56, no. 18, pp. 5228–5233, 2017.

[35] J. Ma, H. Liu, H. Zhan, P. Lin, and Y. Du, "Effects of chlorophyll on upper ocean temperature and circulation in the upwelling regions of the South China Sea," *Aquatic Ecosystem Health Manage.*, vol. 15, no. 2, pp. 127–134, Apr. 2012.

[36] C. Tseng, G. T. F. Wong, I. I. Lin, C. Wu, and K. Liu, "A unique seasonal pattern in phytoplankton biomass in low-latitude waters in the South China Sea," *Geophys. Res. Lett.*, vol. 32, no. 8, 2005, Art. no. L08608.

[37] W. Xu et al., "Mesoscale eddy modulation of subsurface chlorophyll maximum layers in the South China Sea," *J. Geophys. Res., Biogeosci.*, vol. 128, no. 11, Nov. 2023, Art. no. e2023JG007648.

[38] Y. Chen, Q. P. Li, and J. Yu, "Submesoscale variability of subsurface chlorophyll—A across eddy-driven fronts by glider observations," *Prog. Oceanogr.*, vol. 209, Dec. 2022, Art. no. 102905.

[39] Y. Jie et al., "Vertical distribution of summer chlorophyll a concentration in the middle South China Sea," *South China Fisheries Sci.*, vol. 12, no. 4, pp. 1–8, 2016.

[40] L. Ma et al., "Responses of phytoplankton communities to the effect of internal wave-powered upwelling," *Limnology Oceanogr.*, vol. 66, no. 4, pp. 1083–1098, Apr. 2021.

[41] P. Chen, C. Jamet, and D. Liu, "LiDAR remote sensing for vertical distribution of seawater optical properties and Chlorophyll–A from the East China Sea to the South China Sea," *IEEE Trans. Geosci. Remote Sens.*, vol. 60, 2022, Art. no. 4207321.

[42] Q. Liu et al., "Relationship between the effective attenuation coefficient of spaceborne LiDAR signal and the IOPs of seawater," *Opt. Exp.*, vol. 26, no. 23, pp. 30278–30291, 2018.

[43] M. Barbieux et al., "Assessing the variability in the relationship between the particulate backscattering coefficient and the chlorophyll a concentration from a global biogeochemical-argo database," *J. Geophys. Res., Oceans*, vol. 123, no. 2, pp. 1229–1250, Feb. 2018.

[44] R. J. W. Brewin, G. Dall'Olmo, S. Sathyendranath, and N. J. Hardman-Mountford, "Particle backscattering as a function of chlorophyll and phytoplankton size structure in the open-ocean," *Opt. Exp.*, vol. 20, no. 16, pp. 17632–17652, 2012.

[45] C. Zhong, P. Chen, and D. Pan, "An improved adaptive subsurface phytoplankton layer detection method for ocean LiDAR data," *Remote Sens.*, vol. 13, no. 19, p. 3875, Sep. 2021.

[46] F. Rocadenbosch and A. Comerón, "Error analysis for the LiDAR backward inversion algorithm," *Appl. Opt.*, vol. 38, no. 21, pp. 4461–4474, 1999.

[47] H. R. Gordon, "Interpretation of airborne oceanic LiDAR: Effects of multiple scattering," *Appl. Opt.*, vol. 21, no. 16, pp. 2996–3001, 1982.

[48] R. E. Walker and J. W. McLean, "LiDAR equations for turbid media with pulse stretching," *Appl. Opt.*, vol. 38, no. 12, pp. 2384–2397, 1999.

[49] Y. Zhou et al., "Validation of the analytical model of oceanic LiDAR returns: Comparisons with Monte Carlo simulations and experimental results," *Remote Sens.*, vol. 11, no. 16, p. 1870, Aug. 2019.

[50] A. Shapiro, "Monte Carlo sampling methods," in *Handbooks in Operations Research Management Science*, vol. 10. Amsterdam, The Netherlands: Elsevier Science B.V., 2003, pp. 353–425.

[51] S. Chen et al., "SAMC: A novel semi-analytical method for simulating full-polarization LiDAR signals in marine environments," *IEEE Trans. Geosci. Remote Sens.*, vol. 63, 2025, Art. no. 4206716.

[52] S. Chen, P. Chen, W. Kong, R. Shu, and D. Pan, "A semianalytical method for ocean LiDAR radiative transfer considering inelastic and polarized scattering," *IEEE Trans. Geosci. Remote Sens.*, vol. 63, 2025, Art. no. 5700116.

[53] D. Wu, P. Chen, W. Kong, and D. Pan, "A novel semi-analytical method for modeling polarized oceanic profiling LiDAR multiple scattering signals," *IEEE Trans. Geosci. Remote Sens.*, vol. 62, 2024, Art. no. 4203317.

[54] P. Chen, C. Jamet, Z. Mao, and D. Pan, "OLE: A novel oceanic LiDAR emulator," *IEEE Trans. Geosci. Remote Sens.*, vol. 59, no. 11, pp. 9730–9744, Nov. 2021.

[55] Q. Liu et al., "A semianalytic Monte Carlo radiative transfer model for polarized oceanic LiDAR: Experiment-based comparisons and multiple scattering effects analyses," *J. Quant. Spectrosc. Radiat. Transf.*, vol. 237, Nov. 2019, Art. no. 106638.

[56] D. J. Spence, B. R. Neimann, and H. M. Pask, "Monte Carlo modelling for elastic and Raman signals in oceanic LiDAR," *Opt. Exp.*, vol. 31, no. 8, pp. 12339–12348, 2023.
[57] M. Shangguan, Z. Liao, Y. Guo, and Z. Lee, "Seabed backscattered signal peak shift and broadening induced by multiple scattering in bathymetric LiDAR," *IEEE Trans. Geosci. Remote Sens.*, vol. 63, 2025, Art. no. 5701214.
[58] L. R. Poole, D. D. Venable, and J. W. Campbell, "Semianalytic Monte Carlo radiative transfer model for oceanographic LiDAR systems," *Appl. Opt.*, vol. 20, no. 20, pp. 3653–3656, 1981.
[59] H. Yang, K. Yang, Y. Ma, and J. Lin, "Study on LiDAR received backscattering signals using Monte Carlo method," *Proc. SPIE*, vol. 4892, pp. 513–520, May 2003.
[60] Y. Liao, M. Shangguan, Z. Yang, Z. Lin, Y. Wang, and S. Li, "GPU-accelerated Monte Carlo simulation for a single-photon underwater LiDAR," *Remote Sens.*, vol. 15, no. 21, p. 5245, Nov. 2023.
[61] T. Kameda and S. Matsumura, "Chlorophyll biomass off sanriku, Northwestern pacific, estimated by ocean color and temperature scanner (OCTS) and a vertical distribution model," *J. Oceanogr.*, vol. 54, no. 5, pp. 509–516, Sep. 1998.
[62] A. Morel and L. Prieur, "Analysis of variations in ocean color 1," *Limnology Oceanogr.*, vol. 22, no. 4, pp. 709–722, 1977.
[63] Z. Lee and J. Tang, "The two faces of 'case-1' water," *J. Remote Sens.*, vol. 2022, pp. 709–722, Jan. 2022.
[64] Z. Lee et al., "Hyperspectral absorption coefficient of, 'pure seawater in the range of 350–550 nm inverted from remote sensing reflectance," *Appl. Opt.*, vol. 54, no. 3, pp. 546–558, 2015.
[65] L. Prieur and S. Sathyendranath, "An optical classification of coastal and oceanic waters based on the specific spectral absorption curves of phytoplankton pigments, dissolved organic matter, and other particulate materials1," *Limnol. Oceanogr.*, vol. 26, no. 4, pp. 671–689, Jul. 1981.
[66] A. Morel, "Optical properties of pure water and pure seawater," *Opt. aspects Oceanogr.*, 1974.
[67] A. Morel, "Optical properties of pure water and pure seawater," in *Optical Aspects of Oceanography*, N. G. Jerlov and E. S. Nielsen, Ed., London, U.K.: Academic, 1974, pp. 1–24.
[68] M. Muñoz-Anderson et al., "Fitting vertical chlorophyll profiles in the California current using two Gaussian curves," *Limnol. Oceanogr., Methods*, vol. 13, no. 8, pp. 416–424, Aug. 2015.
[69] X. Wenlong et al., "Vertical variability of chlorophyll a concentration and its responses to hydrodynamic processes in the northeastern South China Sea in summer," *J. Tropical Oceanogr.*, vol. 37, no. 5, pp. 62–73, 2018.
[70] Y. Masuda et al., "Photoacclimation by phytoplankton determines the distribution of global subsurface chlorophyll maxima in the ocean," *Commun. Earth Environ.*, vol. 2, no. 1, p. 128, Jun. 2021.
[71] J. H. Churnside and P. L. Donaghay, "Thin scattering layers observed by airborne LiDAR," *ICES J. Mar. Sci.*, vol. 66, no. 4, pp. 778–789, May 2009.
[72] P. Westfeld, H.-G. Maas, K. Richter, and R. Weiß, "Analysis and correction of ocean wave pattern induced systematic coordinate errors in airborne LiDAR bathymetry," *ISPRS J. Photogramm. Remote Sens.*, vol. 128, pp. 314–325, Jun. 2017.

Mingjia Shangguan received the Ph.D. degree from the University of Science and Technology of China, Hefei, China, in 2017.

He is currently an Associate Professor at the State Key Laboratory of Marine Environmental Science, College of Ocean and Earth Sciences, Xiamen University, Xiamen, China. He has authored or co-authored more than 45 peer-reviewed journal articles and holds 51 Chinese national invention patents, as well as one U.S. patent. His main research interests focus on single-photon lidar and its applications in marine environments, atmospheric sensing, and target imaging.

Yirui Guo received the bachelor's degree from Xiamen University, Xiamen, Fujian, China, in June 2024, where she is currently pursuing the master's degree with the State Key Laboratory of Marine Environmental Science, College of Ocean and Earth Sciences.

Her main research area is the retrieval of optical parameters using ocean lidar.

Zhongping Lee (Member, IEEE) was born in China in 1964. He received the Ph.D. degree in physical oceanography from the University of South Florida, Tampa, FL, USA, in 1994, specializing in ocean color remote sensing.

He is currently a Tang Shifeng Chair Professor with Xiamen University, Xiamen, China. His research interests include radiative transfer in the aquatic environment, algorithms of ocean color remote sensing, and applications of satellite ocean color products. He has authored or co-authored more than 190 journal articles in this field.

Dr. Lee is a fellow of the Optical Society of America.

Xiaoquan Song received the B.S. and Ph.D. degrees from the Ocean University of China, Qingdao, China, in 1998 and 2003, respectively.

He is currently with the College of Marine Technology, Faculty of Information Science and Engineering, Ocean University of China. His work broadly concentrates on lidar remote sensing of atmospheric aerosol and wind field, and the development and data analysis of oceanic lidar and atmospheric lidar.

Yan He received the M.Sc. degree from the Ocean University of China, Qingdao, China, in 2003, and the Ph.D. degree from Shanghai Institute of Optics and Fine Mechanics, Chinese Academy of Sciences, Shanghai, China, in 2008.

He is currently a Researcher of spatial information with Shanghai Institute of Optics and Fine Mechanics, Chinese Academy of Sciences. His main research interests include the development of airborne lidar bathymetry systems.